Effects of Fetal Development on Umbilical Artery Hemodynamics: A Computational Fluid Dynamics Study with Doppler Ultrasound

Xue Song[1,2], Jingying Wang[1,*], Guoxiang Li[1,*], Shiyue Zhang[1], Mingrui Li[1] and Chunhian Lee[1,3]

[1] School of Nuclear Science, Energy and Power Engineering, Shandong University, Jinan, 250061, China

[2] Department of Ultrasound, Jinan Central Hospital, Jinan, 250013, China

[3] School of Aeronautic Science and Engineering, Beihang University, Beijing, 100191, China

INFORMATION

Keywords:
Umbilical artery
fetal development
hemodynamics
computational fluid dynamics

DOI: 10.23967/j.rimni.2025.10.69959

SCIPEDIA Revista Internacional de Métodos Numéricos para Cálculo y Diseño en Ingeniería

Revista Internacional Métodos numéricos para cálculo y diseño en ingeniería RIMNI

In cooperation with CIMNE

Effects of Fetal Development on Umbilical Artery Hemodynamics: A Computational Fluid Dynamics Study with Doppler Ultrasound

Xue Song[1,2], **Jingying Wang**[1,*], **Guoxiang Li**[1,*], **Shiyue Zhang**[1], **Mingrui Li**[1] and **Chunhian Lee**[1,3]

[1]School of Nuclear Science, Energy and Power Engineering, Shandong University, Jinan, 250061, China

[2]Department of Ultrasound, Jinan Central Hospital, Jinan, 250013, China

[3]School of Aeronautic Science and Engineering, Beihang University, Beijing, 100191, China

ABSTRACT

The umbilical artery (UA) plays a vital role in the exchange of substances between the mother and fetus through fetal circulation. *In silico* computational fluid dynamics (CFD) has emerged as an effective tool for simulating and analyzing UA blood flow, especially when combined with clinical Doppler ultrasound data. However, most existing studies have applied CFD to investigate UA hemodynamics only at isolated stages of gestation. In reality, UA hemodynamics undergoes continuous changes throughout fetal morphogenesis and physiological development during the entire gestational period. To address this gap, the present study employs CFD to investigate the evolution of UA hemodynamics across eight consecutive gestational age groups: 19, 23, 25, 27, 30, 33, 36, and 39 weeks. The simulations are based on Doppler ultrasound data acquired from clinical examinations of fetuses. The results demonstrate that UA blood flow velocity, secondary helical flow intensity, pressure drop, and wall shear stress generally increase with advancing gestational age. Furthermore, statistical analysis of clinical data across different gestational weeks reveals that the ratio of the Dean number to the Reynolds number (i.e., square root of the dimensionless curvature) remains basically stable during fetal development, with a value of 0.57 ± 0.06. This finding offers new insight into the scaling behavior of UA flow dynamics and may serve as a useful reference for clinical assessments. Overall, this CFD-based investigation provides a comprehensive characterization of UA hemodynamic development and may assist clinicians in gaining a deeper understanding of fetal circulatory adaptation throughout gestation.

OPEN ACCESS

Received: 04/07/2025

Accepted: 10/10/2025

Published: 15/12/2025

DOI
10.23967/j.rimni.2025.10.69959

Keywords:
Umbilical artery
fetal development
hemodynamics
computational fluid dynamics

1 Introduction

The global decline in fertility constitutes a major public health concern and is reflected in the rise in the number of fetal ultrasound examinations and the rise in attention paid to the examination [1]. Therefore, it is imperative to monitor of umbilical arterial hemodynamics throughout pregnancy and to detect more changes. Fetal development is a sophisticated and multifaceted biological process that commences with the fertilization of the ovum, progressing through a series of intricate morphological

*Correspondence: Jingying Wang, Guoxiang Li (wjy_sdu@sdu.edu.cn, liguox@sdu.edu.cn).

and physiological stages, culminating in the emergence of a fully-formed individual [2], which usually takes about 40 weeks. During the initial 8 weeks of embryonic development, the fertilized ovum undergoes cellular division and differentiation, leading to the formation of rudimentary organs and systems. From the 9th week until parturition, various organ systems mature in accordance with their intrinsic developmental patterns, preparing for the birth of the fetus. Throughout the pregnancy, fetal weight and length continue to increase [3].

The umbilical cord (UC) constitutes an essential genetic and physiological component of the fetal system [4–6]. By the 8th week of embryonic development, the UC has completed its fundamental morphogenesis and continues to elongate in conjunction with fetal growth until it is severed at birth. The UC typically encompasses one umbilical vein (UV) and two umbilical arteries (UAs), serving as the vital blood vessel between fetus and placenta. This structure is instrumental in facilitating gas exchange, nutrient provision, and waste elimination between mother and fetus. The integrity of the UC directly affects fetal growth and development [7,8]. Any complications, such as cord compression, knots, or restricted blood flow, can impact the fetus [9]. Monitoring UC blood flow enables clinicians to evaluate fetal well-being, encompassing cardiac function (e.g., [10]) and placental function (e.g., [11]). In clinical practice, the hemodynamics of the umbilical artery (UA) is monitored by ultrasound technology, using indicators such as the systolic/diastolic (S/D) ratio, resistance index (RI), and pulsatility index (PI) [12], as shown in Fig. 1.

Currently, a variety of approaches have been utilized to explore the hemodynamic characteristics of the UA, including clinical observation, *in vitro* experimental investigation, and computational fluid dynamics (CFD) simulation [13–16]. Among these approaches, ultrasonography, as a routine clinical method for evaluating umbilical cord function, remains the most direct and essential technique for investigating the hemodynamic characteristics of the UA. Upon identification of cord-related abnormalities, clinicians typically initiate timely therapeutic strategies and carefully consider optimal delivery timing. Despite its widespread use and advantages—namely its non-invasive nature and real-time feedback—conventional ultrasound still suffers from notable limitations. Specifically, its ability to quantitatively characterize complex hemodynamic features are restricted [17,18]. Furthermore, the diagnostic reliability of ultrasonography is highly dependent on operator expertise, introducing subjectivity and compromising both consistency and repeatability of measurements. In contrast, *in vitro* experimental techniques such as particle image velocimetry (PIV) offer enhanced precision in capturing detailed flow parameters under well-controlled conditions. These methods reduce biological risk and allow for high-resolution visualization of fluid motion. However, replicating the helical architecture of the umbilical artery poses significant challenges for optical access and accurate flow field reconstruction. Additionally, *in vitro* models often involve substantial experimental costs and may not fully replicate physiological flow conditions encountered *in vivo*. With the advancement of computational fluid dynamics (CFD), this method has emerged as a crucial tool for studying hemodynamics *in silico* way [19–22], which provides comprehensive insights into blood flow patterns [23–27]. Its free settings, controlled conditions, group scalability, cost-efficiency, and noninvasive nature have made it widely applicable in cardiovascular research [28–31]. In recent years, CFD has been extensively applied to the study of fetal UA hemodynamics, providing more comprehensive blood flow parameters compared to traditional Doppler ultrasound, such as blood flow velocity, pressure and WSS, to describe blood flow changes under different physiological and pathological conditions. Through CFD, researchers have been able to explore the evolving blood flow patterns in the UA, offering a powerful supplementary tool for monitoring fetal health and early identification of pregnancy complications [13,32–35].

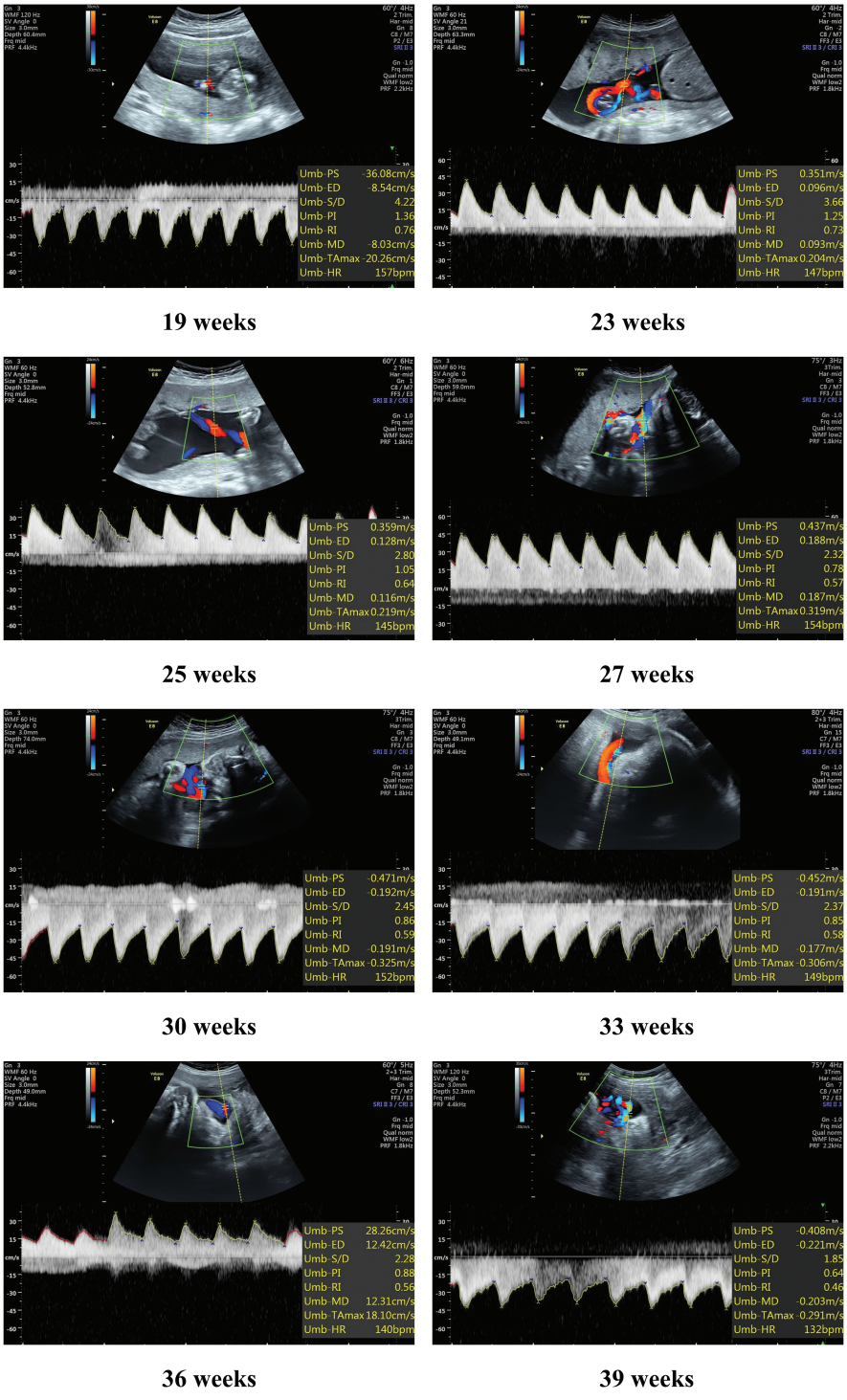

Figure 1: Representative ultrasound images of the UC between 19 to 39 weeks

Early studies have shown that the helical geometry of the UA significantly influences hemodynamics. Kaplan et al. [36] used CFD to simulate blood flow in the UA at 40 weeks of gestation and

found that increased helical coils significantly raised the driving pressure and WSS, while increasing the pitch helped lower these parameters. Saw et al. [33] combined ultrasound and CFD to analyze the WSS distribution in the UA and UV at 32 to 33 weeks, highlighting the critical role of helical geometry in regulating the WSS of the UA, while the WSS in the UV was mainly related to diameter changes. Shah et al. [34] used CFD modeling to analyze the impact of the umbilical cord index (UCI), length, and diameter on the blood flow dynamics at 40 weeks, finding that a high UCI or small diameter significantly increased the pressure gradient and WSS. Kasiteropoulou et al. [32] conducted a CFD analysis at 38 to 40 weeks and investigated the role of the UV and spiral UA in fetal-maternal heat exchange, revealing the critical role of UA helical geometry in regulating blood temperature. Recent studies have gradually focused on the hemodynamic differences between normal and intrauterine growth restriction (IUGR) fetuses. Saw et al. [13] compared blood flow dynamics between normal and IUGR fetuses between 27 and 39 weeks, finding that the WSS trends in the IUGR UA and UV were similar to those of normal fetuses. Wen et al. [35] analyzed the impact of different helical geometries and S/D ratios on the blood flow dynamics at 25 to 30 weeks, showing that a high UCI significantly enhanced WSS, with more uneven WSS distribution in IUGR cases. Song et al. [37] focused on the 24–28 week fetuses and analyzed three typical states of IUGR development, revealing that the hysteresis effect between pressure drop and blood flow velocity could serve as a new indicator for IUGR assessment.

Although the existing studies have significantly contributed to the understanding of UA hemodynamics, the majority have been confined to discrete gestational periods, investigating the impact of anomalous morphological alterations on hemodynamics or comparing normal and pathological groups. The gestational weeks involved are mostly concentrated in the third trimester, with a small span of 2 to 12 weeks. However, the hemodynamic characteristics of the UA change significantly over the entire gestational period. The dynamic changes in UA hemodynamics during the whole period remain underexplored.

The objective of this study is to provide a comprehensive analysis of the evolution of UA hemodynamics during fetal development, using CFD simulations combined with the clinical Doppler ultrasound data of fetuses. Specifically, the analysis focuses on eight consecutively gestational age groups: 19, 23, 25, 27, 30, 33, 36, and 39 weeks. This study covers the full range of gestational weeks for which ultrasound data is available, providing continuous observation of hemodynamic characteristics during fetal development, which has not been discussed in previous computational studies.

2 Materials and Methods

2.1 Ultrasound Image Acquisition

This study included UA datasets from 40 normal fetuses, covering gestational weeks 19, 23, 25, 27, 30, 33, 36, and 39, with five datasets for each week. Data prior to 19 weeks is unavailable because clinical assessments for fetal well-being *in utero* generally do not necessitate Doppler flow velocity waveforms from the UA before this gestational age, making it difficult to collect such data.

Ultrasonic evaluation was performed by several sonographers, using the Voluson E8 ultrasound system (GE Medical Systems Corp., Connecticut, USA) with the C1-5-D, RAB4-8 transducer. Pulse wave Doppler of the UC was obtained in a free loop of UC. Doppler velocity assessments were conducted with an insonation angle of less than 30°. To visually illustrate the data acquisition process, one representative ultrasound image was selected for each gestational week, covering a total of 8 weeks from 19 to 39 weeks of gestation, as shown in Fig. 1. The protocol of this study was approved by Jinan Central Hospital Research Ethics Committee (reference number: R20231226011). Written consents

were obtained from pregnant women from the Jinan Central Hospital. All mothers were healthy, and there was no evidence of fetal abnormalities.

2.2 Geometric Models and Boundary Conditions

Doppler Ultrasound imaging reveals that the longitudinal section of the UC displays two UAs and one UV arranged in a spiral pattern [38]. Fig. 2 is a schematic diagram of the spiral winding of UC and UA, where blue represents UV and red represents UA. A thin layer of Wharton's jelly fills the space between the UC and the UA [39].

Figure 2: Spiral winding diagram of UA and UC

Previous studies have typically modeled the UA as helical tube and assumed circular cross-sections for both the UA and UV [32,34,37], as shown in Fig. 3. In this study, the geometric structure of the UA is similarly treated as a helical circular tube, with key geometric parameters including the helical radius, UC length, and helical pitch. Meanwhile, during the modeling process, the thin Wharton's jelly between the UA and UC is ignored, and the possibility of overlap between the two UAs is not considered, as shown in Fig. 2. The helical radius (R_r) is determined by the radii of the UA and UV, calculated as follows:

$$R_r = R_A + R_V, \tag{1}$$

where R_A is the radius of UA, and R_V is the radius of UV. The UC length and UCI are important clinical reference data. The definition of UCI is as follows:

$$UCI = \frac{U}{L}, \tag{2}$$

where U represents the number of UA coils, and L is the UC length (in cm). From this, the helical pitch (P_h) of the UA can be calculated as:

$$P_h = \frac{L}{U}. \tag{3}$$

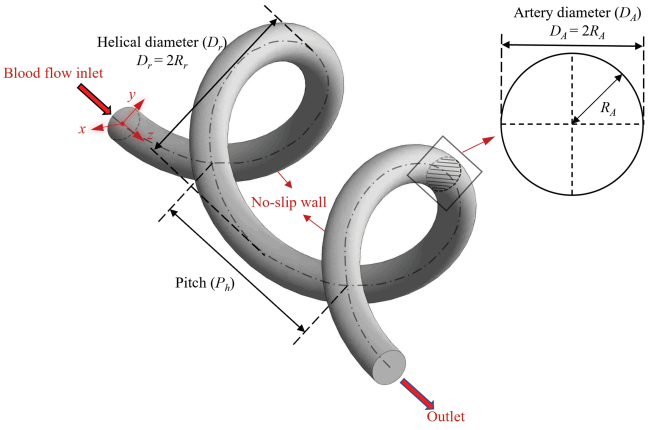

Figure 3: The UA schematic model and boundary conditions, showing only the two spirals

The normalized helical radius (k) of the UA is defined as:

$$k = \frac{R_{\mathrm{A}}}{R_{\mathrm{r}}}. \tag{4}$$

This study focuses on eight gestational weeks between 19 and 39 weeks, with five fetal UC datasets for each week, totaling 40 cases. Based on these datasets, 40 patient-specific UA models are constructed. The parameters of the patient-specific UA geometric models include the UV radius, UA radius, and *UCI*, all of which are derived from the clinical Doppler Ultrasound data. Among the 40 patient-specific UC datasets, the shortest UC length is 15 cm. Therefore, in all simulations, the UC length is uniformly set to 15 cm to ensure that the simulated length is not shorter than the actual UC length. Table 1 provides a sample of geometric parameters from one case for each gestational week group.

Table 1: Sample parameters from one case for each gestational week group

Case	Gestational age (week)	Vein radius (mm)	Artery radius (mm)	Inlet velocity (m/s)
(a)	19	1.80	1.03	0.11
(b)	23	2.21	1.23	0.13
(c)	25	2.13	1.24	0.12
(d)	27	3.70	1.84	0.15
(e)	30	3.86	1.77	0.16
(f)	33	3.81	1.69	0.18
(g)	36	3.77	1.76	0.21
(h)	39	4.30	1.93	0.22

Using the above parameters, the 3D reconstruction is performed by feature sweeping after the baseline is drawn in SolidWorks 2022 software (Dassault Systèmes, Corp., Suresnes, France). The geometric diagram shown in Fig. 3 shows the two helical structures of the UA along the z-axis. The construction methods for the 40 patient-specific UA models are identical.

The setup of boundary conditions directly affects the accuracy of the numerical simulation results. Fig. 3 shows the boundary condition setup for the UAs. The surface of the UA is set as a no-slip wall with zero velocity. The UA end connected to the fetus is set as the inlet with a velocity inlet boundary condition. The inlet velocities for the 40 patient-specific UA models are derived from clinical Doppler ultrasound spectra. Table 1 provides a sample of inlet velocity from one case for each gestational week group. The placental end of the UA is designated as the outlet boundary with a prescribed pressure condition of 2666.44 Pa (20 mmHg), consistent with published physiological data by Shah et al. [34], accurately replicating the real pressure environment at the fetal placental interface.

2.3 Governing Equations

Blood is a non-Newtonian fluid with shear-thinning properties. This work uses the Carreau model to calculate its viscosity as follows [40]:

$$\mu = \mu_\infty + (\mu_0 - \mu_\infty)\left[1 + (\lambda\gamma)^2\right]^{\frac{n-1}{2}}, \tag{5}$$

where μ is the dynamic viscosity of blood; λ is the time constant; n is the power exponent; μ_0 is the zero shear viscosity; and μ_∞ is the infinite shear viscosity. The model parameters are set as $\lambda = 3.313$ s, $n = 0.3568$, $\mu_0 = 0.056$ Pa·s, $\mu_\infty = 0.00345$ Pa·s. γ is the local shear rate, expressed as follows:

$$\gamma = \left(\sum_i \sum_j \gamma_{ij}\gamma_{ji}\right)^{\frac{1}{2}}, \tag{6}$$

where γ_{ij} is the shear rate tensor, expressed as follows:

$$\gamma_{ij} = \frac{1}{2}\left(\frac{\partial v_i}{x_j} + \frac{\partial v_j}{x_i}\right), \tag{7}$$

In the three-dimensional Cartesian coordinate system, the subscript i or $j = 1, 2, 3$, and the coordinates in the x, y, and z directions are represented as x_1, x_2, and x_3, respectively. The velocity components in the x, y, and z directions are represented as v_1, v_2, and v_3, respectively. Since this work focuses on comparing the hemodynamic characteristics of fetuses in different developmental cycles, the steady state model is used. Therefore, the UA blood flow can be characterized by the steady, viscous and incompressible Navier-Stokes equations as follows [41]:

$$\begin{cases} \nabla \cdot \vec{V} = 0 \\ \rho \vec{V} \cdot \nabla \vec{V} = -\nabla p + \nabla \cdot \vec{\tau}, \end{cases} \tag{8}$$

where "∇" is the gradient operator; $\vec{V}$ is the blood fluid velocity vector; p is the pressure; ρ is the blood density with the value of 1060 kg/m^3; $\vec{\tau}$ is the viscous stress tensor as a function of velocity:

$$\vec{\tau} = \mu\left[\nabla \vec{V} + \left(\nabla \vec{V}\right)^T\right], \tag{9}$$

where the superscript "T" represents the transposition.

In the present study, the Reynolds number (Re) is defined as follows:

$$Re = \frac{\rho V_{\mathrm{m}} D\mathrm{A}}{\mu_a}, \tag{10}$$

where D_{A} is the diameter of UA, V_{m} is the mean speed of the blood flow in the UA, and μ_{a} is spatially averaged viscosity within the UA. Previous studies have shown that blood flow in the UA is incompressible laminar flow [13,14,37]. Therefore, all simulations in this study assume laminar flow. Based on the following CFD results, the minimum value of μ_{a} for all cases is about 0.0037 Pa·s, and the corresponding Re is 241. This confirms that the laminar hypothesis in this paper is reasonable.

2.4 Grid Refinement Study

This study uses a sweeping strategy for meshing for each case, with the inlet as the source. A model of the UA in a patient-specific case at 30 weeks is used as an example. Five sets of grids are drawn from rough to fine. In order to accurately calculate the watershed near the pipe wall (where the velocity gradient is large), we set the maximum thickness of the grid close to the pipeline to not exceed 0.25 mm (less than one twentieth of the pipe diameter), and the thickness of the first few layers of the grid close to the pipe wall is much less than 0.25 mm, about 0.015 mm. Five sets of grids adopt the same local refinement setting. The pressure-based transient solver in Fluent 2022 R2 software (ANSYS, Inc., Canonsburg, PA, USA) is used for all cases. The numerical scheme employs a pressure-velocity coupled algorithm with momentum-based Rhie-Chow flux interpolation, utilizing second-order accurate discretization for both pressure and momentum equations, while computing gradients using the least squares cell-based method. The standard transient formulation is adopted without

non-iterative time advancement, frozen flux formulation, warped-face gradient correction, or high-order term relaxation, ensuring solution accuracy and stability for the hemodynamic simulations. The normalized continuity and velocity both converge to 10^{-10}.

After completing the numerical simulations, the most appropriate mesh is selected by comparing the pressure drop from the inlet to the outlet of the UA and the viscosity at the center of the UA cross-section. The results are shown in Table 2. The relative errors in both pressure drop and viscosity are less than 0.1% for Mesh 4 compared to the finer grids. Mesh 4 satisfies both economy and the ability to perform calculations accurately, as shown in Fig. 4. The other cases are meshed in the same strategy.

Table 2: Number of grids and quantitative analysis

Total number of grids		Pressure drop (Pa)	Relative error (%)	Dynamic viscosity (g/m·s)	Relative error (%)
Mesh 1	1.14×10^5	763.77	0.55	4.56	0.41
Mesh 2	2.02×10^5	768.03	0.44	4.55	0.37
Mesh 3	4.03×10^5	771.41	0.10	4.53	0.29
Mesh 4	8.00×10^5	770.66	0.03	4.52	0.05
Mesh 5	1.74×10^6	770.88	–	4.51	–

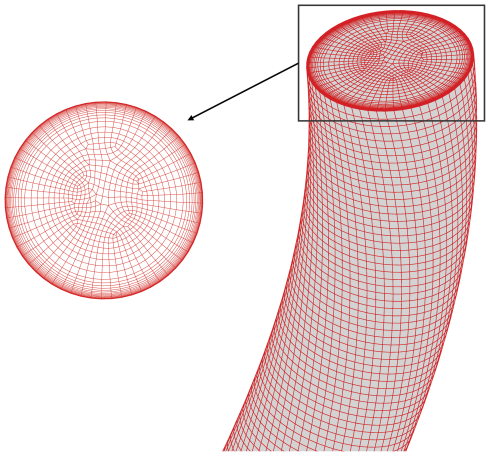

Figure 4: Example of the grid used in this work

3 Results

3.1 Velocity

In this section, the velocity values are nondimensionalized using the mean flow velocity over one cardiac cycle of the 39-week UA model (velocity ratio).

After visualizing the simulation results, it is observed that the blood flow becomes fully developed after the initial helical segment, and stable flow structures form in the downstream region, as shown in Figs. 5 and 6.

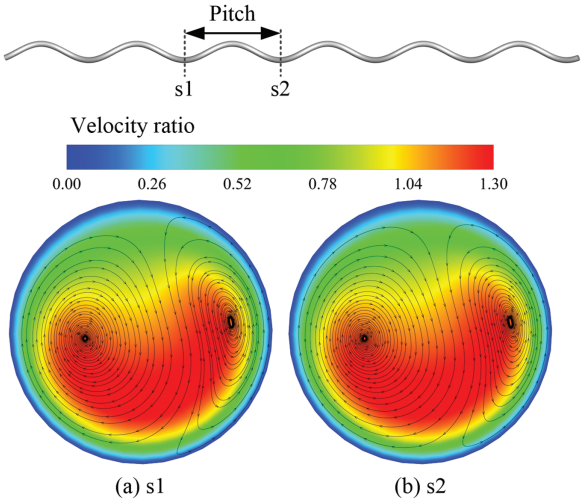

Figure 5: Velocity magnitude and streamlines at two adjacent cross-sections ((a) s1 and (b) s2) within one helical pitch of the UA at 36 weeks

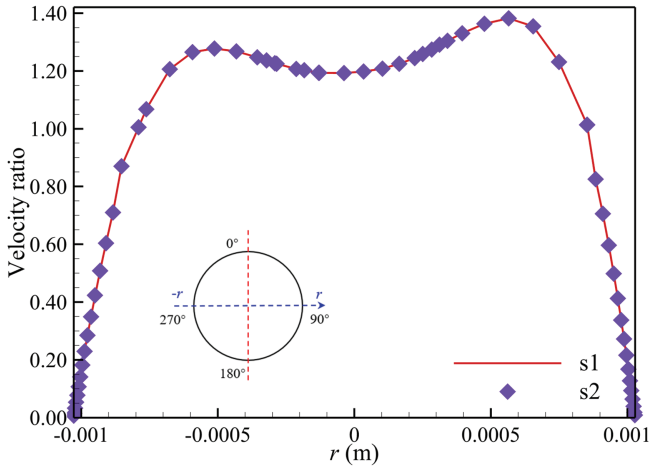

Figure 6: Velocity profiles at s1 and s2 for the 36-week UA model

Fig. 7 illustrates the spatial position of the selected helical segment, which is centered on the middle cross-section s3 and extends by half a helical turn upstream and downstream. This segment is therefore referred to as the mid-helical segment. Fig. 7 also shows the arrangement of short-axis slices used for flow visualization. Each short-axis cross-section is a standardized circular profile, consistent with the geometry of the inlet section.

Fig. 8 presents the blood flow streamlines in the mid-helical segment of the fetal UA from 19 to 39 gestational weeks. A representative case is selected for each gestational week to illustrate the evolution of UA blood flow velocity during fetal development. As gestational age increases, the velocity of blood flow within the UA also increases. Influenced by the helical geometry of the UA, the streamlines do not symmetrically follow the geometric central axis but deviate according to changes in vascular curvature, resulting in an asymmetric velocity distribution. With advancing gestation, the degree of flow deviation toward the helical wall increases. In early gestation (e.g., at 19 weeks), the streamlines

appear relatively regular, although slight deviations induced by the helical structure are already observable. As gestational age increases, this deviation becomes progressively more pronounced.

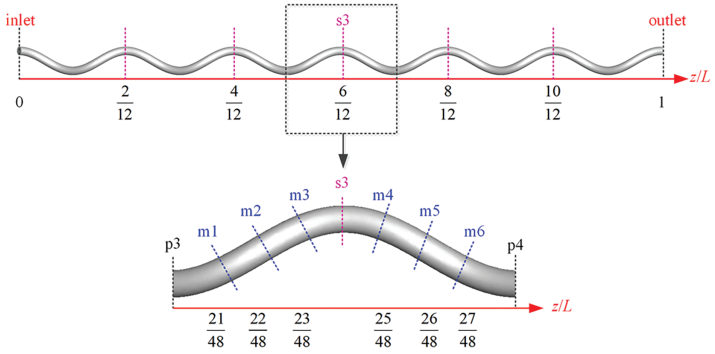

Figure 7: The schematic diagram illustrates the spatial configuration of the mid-segment spiral in the UA and the distribution of equidistant short-axis cross-sections

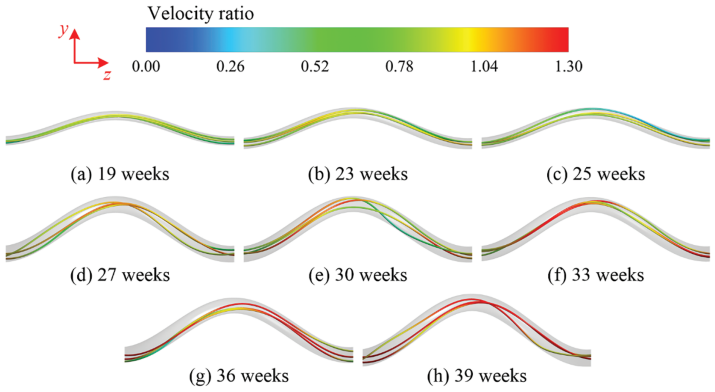

Figure 8: Streamline diagrams of umbilical artery blood flow for representative cases in each gestational week group. (a) 19 weeks; (b) 23 weeks; (c) 25 weeks; (d) 27 weeks; (e) 30 weeks; (f) 33 weeks; (g) 36 weeks; (h) 39 weeks

Fig. 9 shows the cross-sectional velocity distribution in the mid-helical segment of the UA for representative cases from 19 to 39 gestational weeks, further illustrating the spatial heterogeneity of blood flow velocity in the fetal UA across different gestational stages. As gestation progresses, the blood flow velocity within the UA gradually increases. In early fetal development, the UA exhibits relatively low flow velocities and mild asymmetry in the cross-sectional velocity distribution, with limited displacement of the high-velocity region. However, as gestational age advances, the inertial effects become more pronounced, causing the high-speed flow to deviate persistently from the vessel centerline and shift toward the UA wall. Consequently, the peak velocity location exhibits an increasingly prominent rotational trend along the circumferential direction of the cross-section.

To further illustrate the characteristics of blood flow velocity distribution in the UA, this section presents the velocity distribution at four typical cross-sections—p3, m2, s3, and m5—within the mid-helical segment. The corresponding nondimensional positions (z/L) of p3, m2, s3, and m5 are 5/12, 22/48, 6/12, and 26/48, respectively. The locations of these cross-sections are shown in Fig. 7. The velocity distributions at four typical cross-sections—p3, m2, s3, and m5—within the mid-helical

segment of the UA are shown in Figs. 10 and 11. As gestational age advances, the blood flow velocity exhibits a gradual upward trend. Within the current range of velocity ratios (0.00–1.30), during gestational weeks 19–27 (Fig. 10), the proportion of high-velocity regions remains relatively small, and the deviation of peak velocity from the center is not prominent. With further fetal development (Fig. 11), the high-velocity regions expand, the asymmetry in velocity distribution becomes more pronounced, and the rotational trend of the high-speed flow along the circumferential direction becomes increasingly evident across different cross-sections of the mid-helical segment. As blood flows through the UA, centrifugal forces promote the formation of secondary helical flows, generating two counter-rotating vortices of different sizes on the cross-section, as illustrated by the streamlines. During the fetal development period from 19 to 39 weeks, these secondary flow vortices persist, with one vortex consistently larger than the other. In early gestation, the diameter of the larger vortex is only slightly greater than that of the smaller one; however, as gestation progresses, the diameter of the larger vortex increases gradually, and by late gestation, it becomes significantly larger than the smaller vortex.

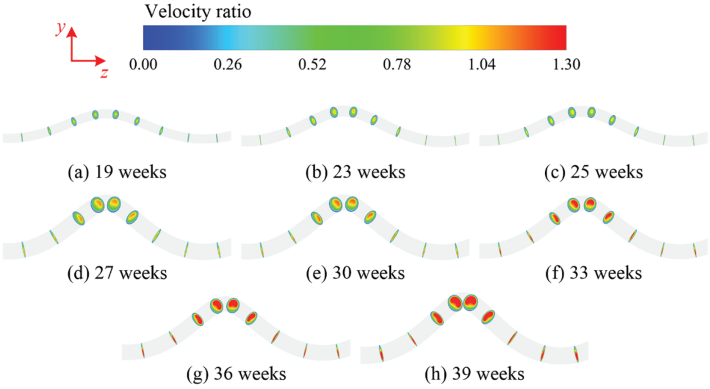

Figure 9: Cross-sectional velocity distribution in the mid-helical segment of the umbilical artery for representative cases of each gestational week group. (a) 19 weeks; (b) 23 weeks; (c) 25 weeks; (d) 27 weeks; (e) 30 weeks; (f) 33 weeks; (g) 36 weeks; (h) 39 weeks

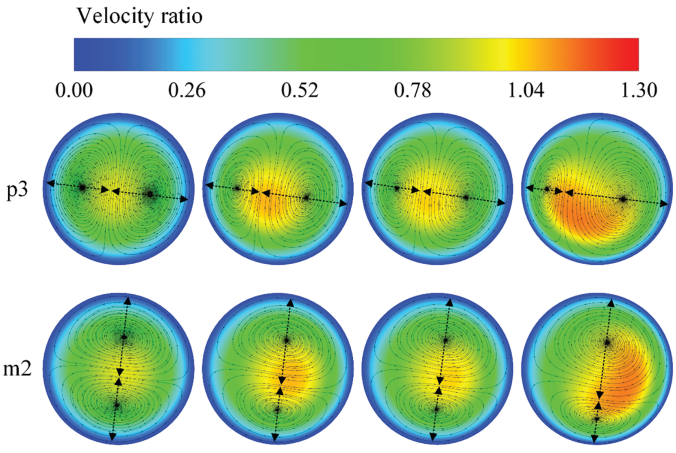

Figure 10: (Continued)

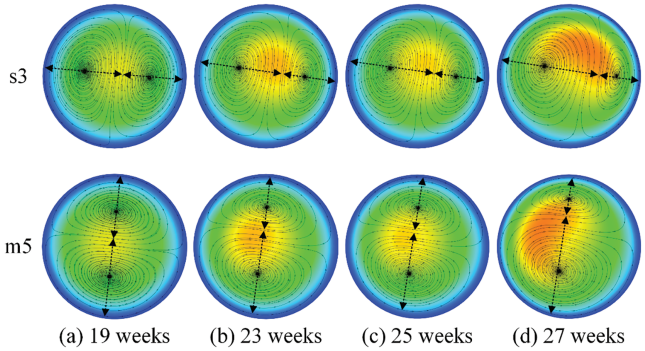

Figure 10: Cross-sectional velocity distributions and streamlines in the mid-helical segment of the umbilical artery for representative cases at 19–27 gestational weeks. (a) 19 weeks; (b) 23 weeks; (c) 25 weeks; (d) 27 weeks

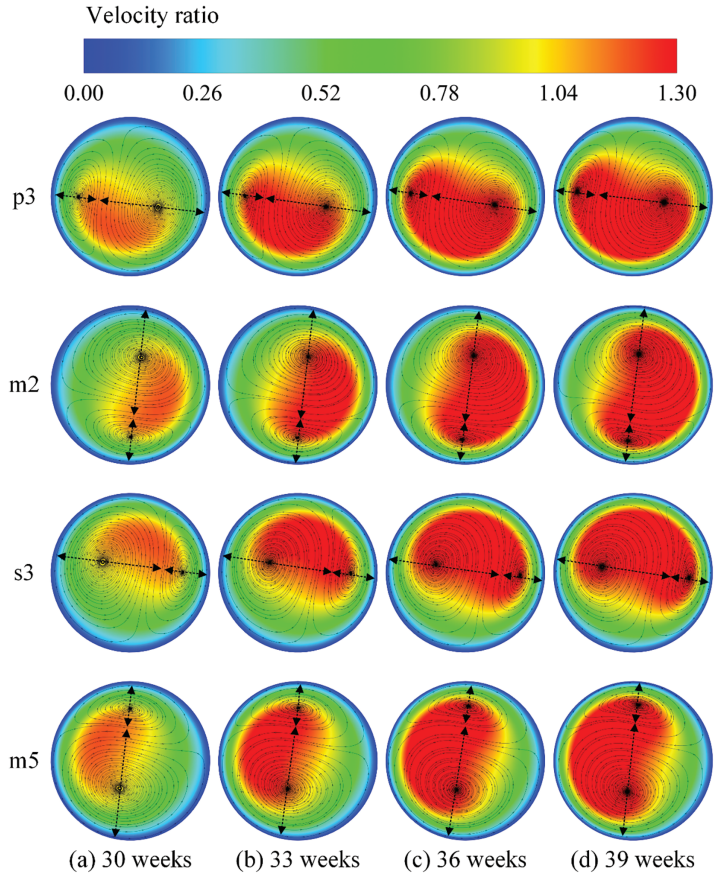

Figure 11: Cross-sectional velocity distributions and streamlines in the mid-helical segment of the umbilical artery for representative cases at 30–39 gestational weeks. (a) 30 weeks; (b) 33 weeks; (c) 36 weeks; (d) 39 weeks

Table 3 presents the nondimensional diameters of the small and large vortices, as well as their ratios (Ratio), at typical cross-sections (Slices) in the mid-helical segment of the UA across different

gestational weeks. The diameter of the large vortex generally shows a continuous increase with advancing gestational age, while the diameter of the small vortex tends to gradually decrease. The ratio of the small to large vortex diameters decreases steadily from approximately 0.6–0.8 in early gestation to around 0.3–0.4 in late gestation. This declining trend in the diameter ratio indicates that the degree of velocity non-uniformity in the UA blood flow becomes progressively more pronounced as gestation advances.

Table 3: Diameters of the small and large vortices and their ratio (Ratio) at mid-helical cross-sections (Slice) of the umbilical artery for representative cases (Week) across gestational ages (D_m denotes the cross-sectional diameter of the UA, and m represents different gestational week cases)

Slice	Week	Small	Large	Ratio	Week	Small	Large	Ratio
p3	19	$0.42D_1$	$0.51D_1$	0.82	30	$0.26D_5$	$0.66D_5$	0.39
	23	$0.36D_2$	$0.57D_2$	0.63	33	$0.27D_6$	$0.66D_6$	0.40
	25	$0.37D_3$	$0.55D_3$	0.67	36	$0.25D_7$	$0.66D_7$	0.37
	27	$0.25D_4$	$0.68D_4$	0.37	39	$0.25D_8$	$0.68D_8$	0.36
m2	19	$0.42D_1$	$0.52D_1$	0.80	30	$0.26D_5$	$0.66D_5$	0.40
	23	$0.36D_2$	$0.57D_2$	0.64	33	$0.28D_6$	$0.69D_6$	0.41
	25	$0.36D_3$	$0.57D_3$	0.63	36	$0.24D_7$	$0.70D_7$	0.34
	27	$0.27D_4$	$0.66D_4$	0.42	39	$0.24D_8$	$0.71D_8$	0.33
s3	19	$0.41D_1$	$0.53D_1$	0.77	30	$0.27D_5$	$0.66D_5$	0.41
	23	$0.36D_2$	$0.56D_2$	0.65	33	$0.27D_6$	$0.69D_6$	0.39
	25	$0.34D_3$	$0.58D_3$	0.59	36	$0.25D_7$	$0.70D_7$	0.36
	27	$0.27D_4$	$0.67D_4$	0.40	39	$0.24D_8$	$0.72D_8$	0.34
m5	19	$0.43D_1$	$0.54D_1$	0.80	30	$0.26D_5$	$0.68D_5$	0.38
	23	$0.36D_2$	$0.57D_2$	0.63	33	$0.26D_6$	$0.68D_6$	0.39
	25	$0.37D_3$	$0.54D_3$	0.68	36	$0.24D_7$	$0.69D_7$	0.34
	27	$0.26D_4$	$0.68D_4$	0.38	39	$0.25D_8$	$0.71D_8$	0.36

The Reynolds number is a dimensionless number represents the ratio of inertial forces to viscous forces, reflecting the viscous effects of the fluid. According to Eq. (8), the blood flow Reynolds number is calculated using the velocity and dynamic viscosity of the middle cross-section, which is located far from the inlet and outlet. The calculated Reynolds numbers are shown in Fig. 12a. The curve is the average results of the 5 cases for each gestational week, while the error bands indicate the range of variation between the five cases for each week. In the gestational weeks from 19 to 39, the Reynolds number increases with the gestational age. The Reynolds number for the fetal average UA model at 39 weeks is nearly four times that at 19 weeks, but still remains within the laminar flow range.

The secondary helical flow intensity is an important parameter to quantify the strength of secondary helical flow. In this study, the dimensionless Dean number (Dn) is used to represent the intensity of the secondary flow in the spiral UA flow, which is defined as follows [42–44]:

$$Dn = Re\sqrt{k}, \tag{11}$$

where k is the dimensionless curvature, defined in Eq. (4); Re for calculation are chosen from the middle cross-section, which is located away from the inlet and outlet of the UA. The distribution of blood flow Dean number of the UA is shown in Fig. 12a. The curve is the average results of the five cases for each gestational week, while the error bands indicate the range of variation among the five cases for each week. The trends of blood Dean number and Reynolds number are almost identical with gestational age. Specifically, during fetal development, the secondary helical flow intensity in the UA gradually increases as the gestational age progresses, influenced by changes in blood flow velocity and UA diameter. Fig. 12b shows the distribution of Dean number and Reynolds number for the 40 patient-specific UA models (scatter plot). Linear fitting of the scatter data reveals a significant linear correlation between the two numbers, with their ratio (i.e., square root of the dimensionless curvature) remaining basically stable at 0.57 ± 0.06.

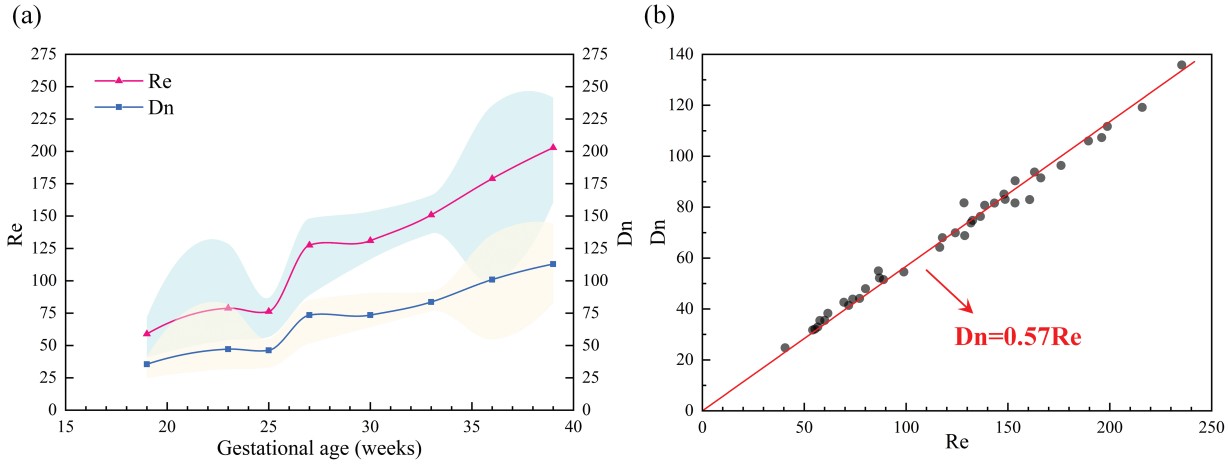

Figure 12: The blood flow Reynolds number (Re) and Dean number (Dn) at the cross-section of the center of the UA for all cases: (a) the variation of Re and Dn with gestational age; the curve is the average result of 5 cases per gestational week, and the error band indicates the distribution range of 5 cases per week. (b) the variation of Dn with Re; the scatter plot is the simulation data, and the curve is the linear fit results

3.2 Pressure

In this chapter, the pressure is nondimensionalized using the mean dynamic pressure (q_d) calculated based on the average flow velocity over one cardiac cycle of the 39-week umbilical artery model, resulting in the dimensionless pressure (Pressure ratio). The dynamic pressure is calculated using the following equation:

$$q_d = \frac{1}{2}\rho V^2, \tag{12}$$

where V is the local blood flow velocity. Fig. 13 presents the pressure distribution at various cross-sections along the mid-helical segment of the UA for representative cases from 19 to 39 gestational weeks (cross-section locations are shown in Fig. 7). Overall, within the displayed range (95–135), the pressure remains nearly uniform across each cross-section. From 19 to 27 weeks, the pressure decreases progressively, while from 27 to 39 weeks, it shows an increasing trend. Fig. 14 shows the wall pressure distribution of the UA for representative cases from 19 to 39 gestational weeks, illustrating the evolution of pressure patterns in the helical UA during fetal development. As shown in Fig. 13,

the pressure is nearly uniformly distributed across the short-axis cross-section. Therefore, the pressure distribution along the vessel wall in the flow direction can represent the overall pressure variation throughout the UA, which mainly manifests as a continuous pressure decrease from the inlet to the outlet. Meanwhile, the pressure levels on the vessel wall are consistent with the variation trends of pressure within the short-axis cross-section.

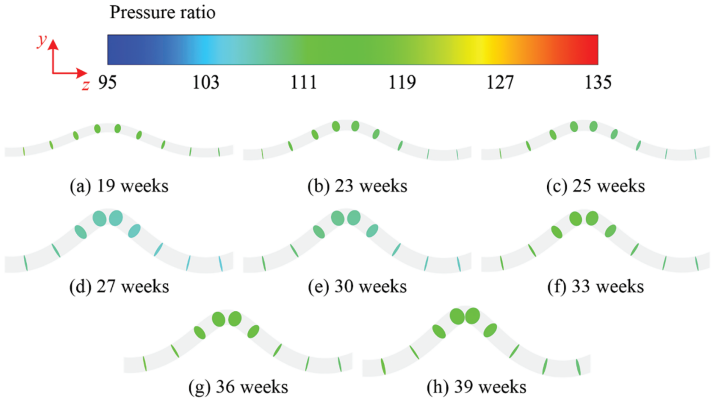

Figure 13: Pressure distribution at the mid-helical cross-sections of the umbilical artery for representative cases of each gestational week group. (a) 19 weeks; (b) 23 weeks; (c) 25 weeks; (d) 27 weeks; (e) 30 weeks; (f) 33 weeks; (g) 36 weeks; (h) 39 weeks

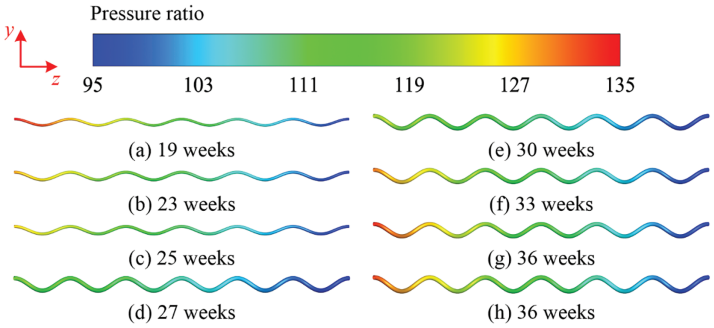

Figure 14: Wall pressure distribution of the umbilical artery for representative cases of each gestational week group. (a) 19 weeks; (b) 23 weeks; (c) 25 weeks; (d) 27 weeks; (e) 30 weeks; (f) 33 weeks; (g) 36 weeks; (h) 39 weeks

The axial pressure distribution along the UA for representative cases of each gestational week group is shown in Fig. 15, illustrating the evolution of axial pressure during fetal development. The horizontal coordinate is nondimensionalized by the UA length, yielding the nondimensional distance (z/L). Between 19 and 39 weeks, after blood flow passes through the first helical segment, the axial pressure distribution generally exhibits an approximately linear decreasing trend. From 19 to 27 weeks, the overall pressure gradually decreases with increasing gestational age, while from 30 to 39 weeks, the pressure increases as gestational age advances. Throughout the 19 to 39 week fetal development period, the pressure drop between the inlet and outlet is greatest at 19 weeks and smallest at 27 weeks.

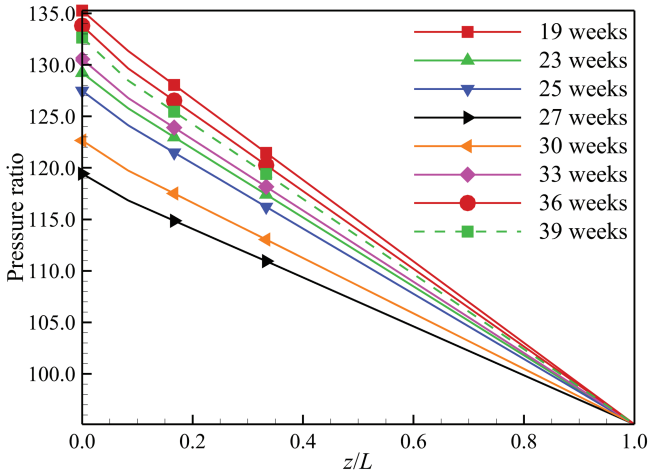

Figure 15: Axial pressure distribution along the umbilical artery for representative cases of each gestational week group

3.3 WSS

The WSS presented in this section is nondimensionalized using the mean dynamic pressure (P_d) calculated based on the average flow velocity over one cardiac cycle of the 39-week umbilical artery model, resulting in the wall shear stress ratio (WSS ratio).

Fig. 16 illustrates the WSS distribution in the fetal UA from 19 to 39 gestational weeks, with a representative case selected for each week to demonstrate the evolution of WSS in the helical UA during fetal development. Observed along the direction of blood flow, the UA exhibits a periodic distribution pattern of WSS throughout fetal development, characterized by alternating regions of high and low shear stress along the vessel wall. As gestational age increases, especially after 30 weeks, the WSS within the UA shows a gradually increasing trend.

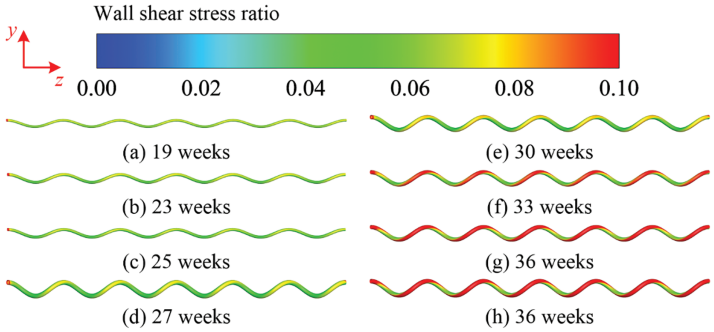

Figure 16: WSS distribution in the umbilical artery for representative cases of each gestational week group. (a) 19 weeks; (b) 23 weeks; (c) 25 weeks; (d) 27 weeks; (e) 30 weeks; (f) 33 weeks; (g) 36 weeks; (h) 39 weeks

Fig. 17 displays the distribution of maximum and minimum WSS at the middle cross-section of the UA. The curves are the average results of the five cases for each gestational week, while the error bands indicate the range of variation among the five cases for each week. From the figure, it can be observed that both the maximum and minimum WSS at the middle cross-section increase with the

advancing gestational weeks, and the range between them gradually expands. As a result, the WSS distribution across the different regions of the UA becomes progressively more uneven. At 39 weeks, the difference between the maximum and minimum WSS reaches 1.9 Pa, which is four times greater than at 19 weeks.

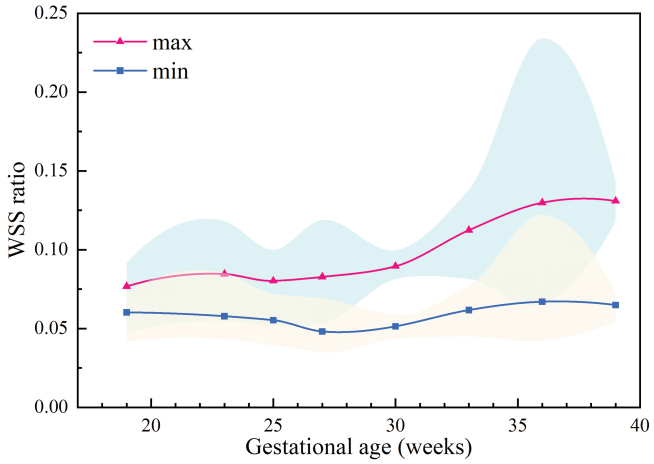

Figure 17: Maximum WSS and minimum WSS at the cross-section of the UA center for all cases. The curve is the average result of 5 cases per gestational week, and the error band indicates the distribution range of 5 cases per week

4 Discussion

This work uses CFD simulations to study the evolution of UA hemodynamics of eight consecutively gestational age groups: 19, 23, 25, 27, 30, 33, 36, and 39 weeks, with 5 cases in each group. The research covers the full range of gestational weeks for which ultrasound data are available and reveals the evolution of the blood flow velocity, pressure, and WSS in the UA during fetal development, which has not been discussed in previous computational studies.

As the gestational period advances, undergoes continuous morphological and physiological changes. Fetal weight and organ volumes increase with advancing gestational weeks, and the diameter of umbilical vessels also enlarges [45–48]. Ultrasound examinations show that blood flow velocity and rate in the UA increase with gestational age, while hemodynamic indices such as the S/D ratio, RI, and PI gradually decrease [49], as shown in Fig. 1. According to CFD simulation results, the UA hemodynamic characteristics during fetal development also exhibit certain patterns of change. The simulations reveal that the blood flow velocity, pressure drop, and WSS in the entire UA generally increase with the growth of gestational age. Calculations further show that the Reynolds number, reflecting blood flow viscous effects, and the Dean number, characterizing secondary helical flow intensity, also increase in the entire UA with gestational age. From 19 to 39 weeks, the Reynolds number ranges from 40 to 242, while the Dean number varies between 24 and 144.

Although significant changes occur in UA hemodynamics during fetal rapid growth, one relatively stable indicator is identified in the study: the ratio of the Dean number to the Reynolds number (i.e., square root of the dimensionless curvature) remains basically stable throughout gestation, with a value of 0.57 ± 0.06. From Eq. (9), it is evident that the ratio of the Dean number to the Reynolds number is related to the dimensionless curvature k, specifically, $\sqrt{k}$. As shown in Eq. (4), k is the ratio of the UA radius to the curvature radius, where the curvature radius is the sum of the UA radius and the

UV radius. The stable characteristic of the dimensionless curvature k during fetal development has important clinical significance. The dimensionless curvature k can be directly calculated by measuring the diameters of the UA and UV through clinical ultrasound, without relying on complex simulations. Therefore, this stable characteristic can provide a convenient and reliable quantitative basis for the rapid clinical assessment of fetal circulatory function. The UAs studied in this work are in normal conditions, suggesting that, under ideal circumstances, as fetal age advances, the radius of the UA increases while the helical radius adjusts to maintain a nearly constant dimensionless curvature. If the UC is too tight, too loose, or knotted, causing changes in the radius of the UA or the spiral radius, it may affect the stability of the k value, thereby disrupting the stable state of blood flow. In severe cases, such as excessive torsion of the cord, true knot of the cord, it will produce a certain pathological state that affects the blood circulation between fetus and placenta, and then affects the growth and development of fetus.

Previous studies have mainly focused on the changes in UA blood flow patterns and suggested that alterations in normal blood flow patterns may indicate pathological conditions such as IUGR, which is typically characterized by increased S/D ratio, RI value and PI value. However, some relatively stable indicators were considered unrelated to disease development, for example Köşüş et al. [50] found a constant average diameter ratio of UV to the UA of 2.11 between 20–40 weeks, which did not vary with gestational age but they concluded that it had no predictive value for complicated pregnancies management either. Our research also identified some similar relatively stable indicators that does not change with gestational weeks during pregnancy, such as the diameter ratio between the small and large vortices in the secondary helical flow (0.43 ± 0.09), the UA laminar state, and the ratio of Dean number to Reynolds number (0.57 ± 0.06). In this study, it is believed that this is necessary to maintain a stable blood flow state under high-speed growth conditions. Once the indicator is not in a stable state, it may suggest that there are potential risks of abnormalities or even direct manifestations of abnormal states. The indicator may serve as important tools for the prediction and management of complicated pregnancies, which could be further studied and developed in the future as an indicator of fetal safety *in utero*.

This study has several limitations. Firstly, the elasticity of the UA is not considered, and the UA is assumed to be a rigid vessel with a uniform circular cross-section. Secondly, the cells in the blood are not considered, and the blood is treated as a homogeneous liquid phase with non-Newtonian properties. Thirdly, the study is based on 40 cases, which is a relatively small sample size. As the research progresses, these factors will be gradually incorporated to make the findings more aligned with real conditions.

In conclusion, this study systematically analyzes the evolution of UA hemodynamic characteristics during fetal development, using CFD combined with clinical Doppler ultrasound. The findings reveal both the dynamic changes and a relatively stable feature of hemodynamic parameters, providing new insights into the progression of blood flow in the fetal development.

Acknowledgement: The authors would like to express their sincere gratitude to all individuals and organizations who contributed to this study. We especially thank Xinglian Yang, Wei Zhao, and Xinyue Dong for their assistance with figure preparation, and Guodong Zhang for his help with manuscript formatting. We appreciate the support and insightful discussions provided by colleagues and collaborators throughout the different stages of the research. Finally, we are grateful to the patients and members of the public who enthusiastically participated as research volunteers, whose support made this study possible.

Funding Statement: This work was supported by the Graduate Education and Teaching Reform Project of Shandong University (Grant No. XYJG2024030), the Laboratory Construction and Management Research Project of Shandong University (Grant No. sy20232305), and the Future Project for the Young Scholars of Shandong University (Grant No. 31380082164048).

Author Contributions: The authors confirm contribution to the paper as follows: study conception and design: Xue Song, Jingying Wang, Guoxiang Li, Chunhian Lee; data collection: Xue Song, Shiyue Zhang, Mingrui Li; analysis and interpretation of results: Xue song, Jingying Wang, Guoxiang Li; draft manuscript preparation: Xue Song, Jingying Wang, Guoxiang Li, Shiyue Zhang, Mingrui Li. All authors reviewed the results and approved the final version of the manuscript.

Availability of Data and Materials: The data that support the findings of this study are available from the corresponding author, J. Wang, upon reasonable request.

Ethics Approval: The study was conducted in accordance with the Declaration of Helsinki and approved by the Ethics Committee of Jinan Central Hospital (approval number: R20231226011). Clinical data were collected from medical records. Fetuses with twin pregnancies, preterm birth, genetic malformations, chromosomal or developmental disorders, hypertension, diabetes, alcohol, nicotine, or drug abuse were excluded from the study. Women with immunological, cardiovascular, gastrointestinal, or pulmonary diseases were also excluded. The clinical data and ultrasound records were accessed for research purposes on 26 November 2024. All data were fully anonymized before analysis, and the authors had no access to identifiable patient information at any stage of the study.

Informed Consent: Informed consent was obtained from all subjects involved in the study.

Conflicts of Interest: The authors declare no conflicts of interest to report regarding the present study.

References

1. Ibrahimi J, Mumtaz Z. Ultrasound imaging and the culture of pregnancy management in low-and middle-income countries: a systematic review. Int J Gynaecol Obstet. 2024;165(1):76–93. doi:10.1002/ijgo.15097.
2. Zhai J, Xiao Z, Wang Y, Wang H. Human embryonic development: from peri-implantation to gastrulation. Trends Cell Biol. 2022;32(1):18–29. doi:10.1016/j.tcb.2021.07.008.
3. Xu Y, Zhang T, Zhou Q, Hu M, Qi Y, Xue Y, et al. A single-cell transcriptome atlas profiles early organogenesis in human embryos. Nat Cell Biol. 2023;25(4):604–15. doi:10.1038/s41556-023-01108-w.
4. Guyton AC, Hall JE. Guyton and hall textbook of medical physiology. 1st ed. Amsterdam, The Netherlands: Elsevier; 2011.
5. Obeagu EI, Obeagu GU. An update on factors affecting umbilical cord care among mothers: a review. Medicine. 2024;103(28):e38945. doi:10.1097/md.0000000000038945.
6. Obeagu EI, Obeagu GU, Musiimenta E, Bot YS, Hassan AO. Update on mothers towards neonatal umbilical cord sepsis: african perspectives. Int J Curr Res Med Sci. 2023;9(2):18–20. doi:10.22192/ijcrms.2023.09.02.004.
7. Song X, Liu C, Wang J, Yang X, Li M. Current perspectives on umbilical cord abnormalities including blood flow parameters based on ultrasound observations. Mol Cell Biomech. 2022;19(4):209–19. doi:10.32604/mcb.2022.026082.
8. Hammad IA, Blue NR, Allshouse AA, Silver RM, Gibbins KJ, Page JM, et al. Umbilical cord abnormalities and stillbirth. Obstet Gynecol. 2020;135(3):644–52. doi:10.1097/aog.0000000000003676.

9. Patel T, Pajai S. True umbilical cord knot leading to fetal distress-an obstetric emergency. J Pharm Res Int. 2021;2021:60–3. doi:10.9734/jpri/2021/v33i35a31878.
10. Tan F, Yang JJ, Shen YQ, Li YFH, Wang HR, Fan SH. Evaluation of normal fetal heart mor-phology and systolic function by fetal heart quantification technique. Chinese J Med Ultrasou. 2023;20(6):598–604. (In Chinese). doi:10.3877/cma.j.issn.1672-6448.2023.06.005.
11. Lian Y. Application of umbilical artery blood flow monitoring in obstetrics. Chinese J Pract Gynecol Obstet. 2022;38(4):392–5. (In Chinese). doi:10.19538/j.fk2022040103.
12. Recker F, Gembruch U, Strizek B. Clinical ultrasound applications in obstetrics and gynecology in the year 2024. J Clin Med. 2024;13(5):1244. doi:10.3390/jcm13051244.
13. Saw SN, Poh YW, Chia D, Biswas A, Mattar CNZ, Yap CH. Characterization of the hemodynamic wall shear stresses in human umbilical vessels from normal and intrauterine growth restricted pregnancies. Biomech Model Mechanobiol. 2018;17(4):1107–17. doi:10.1007/s10237-018-1017-8.
14. Wilke DJ, Denier JP, Khong TY, Mattner TW. Pressure and flow in the umbilical cord. J Biomech. 2018;79(4):78–87. doi:10.1016/j.jbiomech.2018.07.044.
15. Yin Q, Zhang Y, Ma Q, Gao L, Li P, Chen X. The clinical value of blood flow parameters of the umbilical artery and middle cerebral artery for assessing fetal distress. Am J Transl Res. 2021;13(5):5280–6.
16. Baron J, Weintraub AY, Sciaky Y, Mastrolia SA, Speigel E, Hershkovitz R. Umbilical artery blood flows among pregnancies with single umbilical artery: a prospective case-control study. J Matern Fetal Neonatal Med. 2015;28(15):1803–5. doi:10.3109/14767058.2014.968845.
17. Huang C, Zhang W, Gong P, Lok UW, Tang S, Yin T, et al. Super-resolution ultrasound localization microscopy based on a high frame-rate clinical ultrasound scanner: an in-human feasibility study. Phys Med Biol. 2021;66(8):08NT01. doi:10.1088/1361-6560/abef45.
18. Song P, Trzasko JD, Manduca A, Huang R, Kadirvel R, Kallmes DF, et al. Improved super-resolution ultrasound microvessel imaging with spatiotemporal nonlocal means filtering and bipartite graph-based microbubble tracking. IEEE Trans Ultrason Ferroelectr Freq Control. 2018;65(2):149–67. doi:10.1109/tuffc.2017.2778941.
19. Wang J, Huang W, Zhou Y, Han F, Ke D, Lee C. Hemodynamic analysis of VenaTech convertible vena Cava filter using computational fluid dynamics. Front Bioeng Biotechnol. 2020;8:556110. doi:10.3389/fbioe.2020.556110.
20. Li M, Wang J, Huang W, Zhou Y, Song X. Evaluation of hemodynamic effects of different inferior vena Cava filter heads using computational fluid dynamics. Front Bioeng Biotechnol. 2022;10:1034120. doi:10.3389/fbioe.2022.1034120.
21. Wild NC, Bulusu KV, Plesniak MW. Vortex dynamics in healthy and pro-atherogenic carotid artery bifurcation models. Phys Rev Fluids. 2024;9(8):083102. doi:10.1103/physrevfluids.9.083102.
22. Zhang S, Song X, Wang J, Huang W, Zhou Y, Li M. CFD study on hemodynamic characteristics of inferior vena Cava filter affected by blood vessel diameter. Mol Cell Biomech. 2023;20(2):81–94. doi:10.32604/mcb.2023.044445.
23. Geng Y, Liu H, Wang X, Zhang J, Gong Y, Zheng D, et al. Effect of microcirculatory dysfunction on coronary hemodynamics: a pilot study based on computational fluid dynamics simulation. Comput Biol Med. 2022;146:105583. doi:10.1016/j.compbiomed.2022.105583.
24. Jin ZH, Barzegar Gerdroodbary M, Valipour P, Faraji M, Abu-Hamdeh NH. CFD investigations of the blood hemodynamic inside internal cerebral aneurysm (ICA) in the existence of coiling embolism. Alex Eng J. 2023;66:797–809. doi:10.1016/j.aej.2022.10.070.
25. Masoudi A, Ali Pakravan H, Bazrafshan Drissi H. Competitive flow of bilateral internal thoracic artery Y-graft: insights from hemodynamics and transit time flow measurement parameters. Phys Fluids. 2024;36(9):091910. doi:10.1063/5.0222166.

26. Rehman MAU, Ekici Ö. Comparative analysis of mechanical wall shear stress and hemodynamics to study the influence of asymmetry in abdominal aortic aneurysm and descending thoracic aortic aneurysm. Phys Fluids. 2024;36(7):071904. doi:10.1063/5.0216980.
27. Zhao Y, Shi Y, Jin Y, Cao Y, Song H, Chen L, et al. Evaluating short-term and long-term risks associated with renal artery stenosis position and severity: a hemodynamic study. Bioengineering. 2023;10(9):1002. doi:10.3390/bioengineering10091002.
28. Candreva A, De Nisco G, Rizzini ML, D'Ascenzo F, De Ferrari GM, Gallo D, et al. Current and future applications of computational fluid dynamics in coronary artery disease. Rev Cardiovasc Med. 2022;23(11):377. doi:10.31083/j.rcm2311377.
29. Gramigna V, Palumbo A, Rossi M, Fragomeni G. A computational fluid dynamics study to compare two types of arterial cannulae for cardiopulmonary bypass. Fluids. 2023;8(11):302. doi:10.3390/fluids8110302.
30. Pavlin-Premrl D, Boopathy SR, Nemes A, Mohammadzadeh M, Monajemi S, Ko BS, et al. Computational fluid dynamics in intracranial atherosclerosis—lessons from cardiology: a review of CFD in intracranial atherosclerosis. J Stroke Cerebrovasc Dis. 2021;30(10):106009. doi:10.1016/j.jstrokecerebrovasdis.2021.106009.
31. Viola F, Del Corso G, Verzicco R. High-fidelity model of the human heart: an immersed boundary implementation. Phys Rev Fluids. 2023;8(10):100502. doi:10.1103/physrevfluids.8.100502.
32. Kasiteropoulou D, Topalidou A, Downe S. A computational fluid dynamics modelling of maternal-fetal heat exchange and blood flow in the umbilical cord. PLoS One. 2020;15(7):e0231997. doi:10.1371/journal.pone.0231997.
33. Saw SN, Dawn C, Biswas A, Mattar CNZ, Yap CH. Characterization of the *in vivo* wall shear stress environment of human fetus umbilical arteries and veins. Biomech Model Mechanobiol. 2017;16(1):197–211. doi:10.1007/s10237-016-0810-5.
34. Shah RG, Girardi T, Merz G, Necaise P, Salafia CM. Hemodynamic analysis of blood flow in umbilical artery using computational modeling. Placenta. 2017;57(1):9–12. doi:10.1016/j.placenta.2017.05.017.
35. Wen J, Tang J, Ran S, Ho H. Computational modelling for the spiral flow in umbilical arteries with different Systole/Diastole flow velocity ratios. Med Eng Phys. 2020;84:96–102. doi:10.1016/j.medengphy.2020.08.002.
36. Kaplan AD, Jaffa AJ, Timor IE, Elad D. Hemodynamic analysis of arterial blood flow in the coiled umbilical cord. Reprod Sci. 2010;17(3):258–68. doi:10.1177/1933719109351596.
37. Song X, Wang J, Sun K, Lee C. Analysis of umbilical artery hemodynamics in development of intrauterine growth restriction using computational fluid dynamics with Doppler ultrasound. Bioengineering. 2024;11(11):1169. doi:10.3390/bioengineering11111169.
38. Strong TH, Jarles DL, Vega JS, Feldman DB. The umbilical coiling index. Am J Obstet Gynecol. 1994;170(1):29–32. doi:10.1016/s0002-9378(94)70378-7.
39. Wang T, Tao K, Wang W, Ge X, Pei Q. Hemodynamic analysis on the umbilical cord with different coiling and nuchal cord conditions: a computational model-based study. Phys Fluids. 2025;37(2):021904. doi:10.1063/5.0251530.
40. Li M, Song X, Wang J, Zhou Y, Zhang S, Lee C. Simulation study of hemodynamic commonality of umbrella-shaped inferior vena Cava filter using computational fluid dynamics. Phys Fluids. 2024;36(8):081913. doi:10.1063/5.0217997.
41. Lv H, Fu K, Liu W, He Z, Li Z. Numerical study on the cerebral blood flow regulation in the circle of Willis with the vascular absence and internal carotid artery stenosis. Front Bioeng Biotechnol. 2024;12:1467257. doi:10.3389/fbioe.2024.1467257.
42. Chen Y, Xiong Y, Jiang W, Yan F, Guo M, Wang Q, et al. Numerical simulation on the effects of drug eluting stents at different Reynolds numbers on hemodynamic and drug concentration distribution. Biomed Eng Online. 2015;14(Suppl 1):S16. doi:10.1186/1475-925X-14-S1-S16.

43. Ferng YM, Lin WC, Chieng CC. Numerically investigated effects of different Dean number and pitch size on flow and heat transfer characteristics in a helically coil-tube heat exchanger. Appl Therm Eng. 2012;36:378–85. doi:10.1016/j.applthermaleng.2011.10.052.
44. Moulin P, Rouch JC, Serra C, Clifton MJ, Aptel P. Mass transfer improvement by secondary flows: dean vortices in coiled tubular membranes. J Membr Sci. 1996;114(2):235–44. doi:10.1016/0376-7388(95)00323-1.
45. Gallo CBM, Costa WS, Favorito LA, Sampaio FJB. Development of nerves and vessels in the penis during the human fetal period. Int Braz J Urol. 2024;50(6):764–71. doi:10.1590/s1677-5538.ibju.2024.9916.
46. Szpinda M, Paruszewska-Achtel M, Woźniak A, Mila-Kierzenkowska C, Elminowska-Wenda G, Dombek M, et al. Volumetric growth of the liver in the human fetus: an anatomical, hydrostatic, and statistical study. Biomed Res Int. 2015;2015:858162. doi:10.1155/2015/858162.
47. Szpinda M, Siedlaczek W, Szpinda A, Woźniak A, Mila-Kierzenkowska C, Wiśniewski M. Volumetric growth of the lungs in human fetuses: an anatomical, hydrostatic and statistical study. Surg Radiol Anat. 2014;36(8):813–20. doi:10.1007/s00276-014-1269-7.
48. Asghar A, Asad MR, Naaz S, Rani M. Screening of the growth of Thymus of human fetuses. Anat Cell Biol. 2019;52(4):478–85. doi:10.5115/acb.19.094.
49. Pelayo-Delgado I, Gómez-Montes E, Álvaro-Navidad M. Update on second trimester ultrasound scanning in pregnancy. Clínica E Investig En Ginecología Y Obstet. 2025;52(1):100997. doi:10.1016/j.gine.2024.100997.
50. Köşüş A, Köşüş N, Turhan NÖ. Is there any relation between umbilical artery and vein diameter and estimated fetal weight in healthy pregnant women? J Med Ultrason. 2012;39(4):227–34. doi:10.1007/s10396-012-0360-0.